sciendo

Polish Journal of Chemical Technology, 26, 2, 25—30, 10.2478/pjct-2024-0014

Enhanced antireflective and laser damage resistance of refractive-index gradient SiO_2 nanostructured films at 1064 nm

Lili Wan[1], Jie Yang[1], Xiaoru Liu[1], Jiayi Zhu[1, 3, *], Gang Xu[1], Chenchun Hao[1], Xuecheng Chen[2], Zhengwei Xiong[1, *]

[1]Joint Laboratory for Extreme Conditions Matter Properties, School of Mathematics and Physics, Southwest University of Science and Technology, Mianyang 621010, China
[2]Department of Nanomaterials Physicochemistry, Faculty of Chemical Technology and Engineering, West Pomeranian University of Technology, Szczecin, Piastow Ave. 42, 71-065 Szczecin, Poland
[3]Key Laboratory of Icing and Anti/De-icing, China Aerodynamics Research and Development Center, Mianyang 621000, China
[*]*Corresponding authors: e-mail:* jyzhu@swust.edu.cn (Jiayi Zhu), zw-xiong@swust.edu.cn (Zhengwei Xiong)

A facile sol-gel procedure was employed to create refractive-index gradient SiO_2 antireflective (AR) films. A monolayer film, characterized by the porous crosslinking framework, was fabricated with a designed volume ratio mixture both with colloidal silica suspension and soluble organic polysiloxane. The upper layer for the bilayer film was a hexamethylisilazane (HMDS) modified colloidal silica suspension, leading to the film surface transfer to hydrophobic. The strategic design of nanostructures in the bottom and upper layers resulted in a refractive-index gradient SiO_2 film with enhanced AR properties. The bilayer film demonstrated a transmittance of 99.5% at 1064 nm, accompanied by a notable reduction in reflectivity. Moreover, the laser-induced damage threshold of the bilayer film was increased by 30%, rising to as high as 24.7 J/cm^2. The SiO_2 nanostructured film both showed a refractive-index gradient structure with excellent AR properties and exhibited good laser damage resistance.

Keywords: SiO_2 nanostructured films; Sol-gel procedure; Refractive-index gradient; Antireflective; Laser damage resistance.

INTRODUCTION

High-power lasers represent a promising avenue for triggering fusion reactions, offering substantial energy release while avoiding greenhouse gas emissions and toxic radioactive byproducts[1]. However, the multitude of optical components within high-power laser devices result in intense reflection at vacuum-component interfaces, stemming from abrupt changes in refractive index. The laser light reflection not only disrupts target diagnostics and damages optical elements but also significantly diminishes overall laser energy output. To address this great challenge, antireflective (AR) films play a crucial role by reducing light reflection and enhancing light transmission. In high-power laser fusion systems, it is essential to convert fundamental frequency light at 1064 nm into the third harmonic laser before introducing the laser into the target chamber. Consequently, it is pivotal to improve the AR ability of the fundamental frequency light at 1064 nm to minimize laser energy loss in high-power laser fusion systems.

Despite the perfect AR films is highly needed, the achievement is constrained by the absence of materials with a gradient refractive index. Various types of research have been reported to artificially create materials with refractive-index gradient films[2–13]. Emphasizing the significance of precise control over structure depth and shape is crucial to attaining effective antireflective effects[14]. However, it still remains challenging to construct AR films by using refractive-index gradient layers. Transparent multilayer systems offer an alternative approach to reduce reflections by alternating high and low-refractive-index materials[15]. The reflectance of broadband AR films is influenced by the refractive index of the out layer. The antireflective property becomes better due to the lower refractive index of the out layer[16, 17]. However, the limitation persists due to the lack of ultra-low refractive-index materials in nature[18–20]. Previous efforts have predominantly focused on the AR performance in solar photovoltaic devices[21–23]. However, only limited investigations reported the modified AR films at 1064 nm. Yoldas et al. reported a method for depositing a porous SiO_2 AR coating, of which the transmittance reached as high as 99.0% at 1064 nm[24]. However, the preparation method involved cumbersome and time-consuming processes of annealing and etching for the films. Xu group disclosed a bilayer film with refractive indices of both 1.34 and 1.20 for the bottom and upper layers, respectively, achieving a transmittance of 98.58% at 1064 nm in the bilayer films[25]. Nevertheless, the corresponding transmittance at 1064 nm was relatively low, seriously limiting its practical application. Up to now, as far as we know, there has been no report on exceptional AR films featuring a refractive-index gradient nanoarchitecture and an easy fabrication tailored to specific wavelengths, such as 1064 nm, being crucial for high-power laser systems.

Except for achieving low reflectance and high transmittance at 1064 nm, high-power laser systems require AR films with an elevated laser-induced damage threshold (LIDT). Damage induced by laser for AR films is a critical issue, particularly in the vacuum environment where contaminants like organic compounds and moisture are present. Because of the hydrophilic nature, SiO_2-based AR films are prone to adsorbing water or organic compounds, impacting the transmittance and weakening the LIDT. Although efforts have been made to enhance hydrophobic properties, challenges still persist in simultaneously optimizing AR performance at 1064 nm and laser-induced damage resistance of SiO_2-based AR films in high-power laser systems[26–29].

In the present work, these challenges were well addressed by presenting SiO_2–based antireflective films

with well-designed multilayer refractive-index gradient nanostructures. The AR property and LIDT of the monolayer and bilayer film were thoroughly discussed for contributing to the understanding and advancement of SiO_2-based antireflective films in high-power laser applications.

EXPERIMENTAL

Reagents

Absolute ethanol (99.5%), aqueous ammonia solution (26%), tetraethylorthosilicate (TEOS, 98%), and concentrated hydrochloric acid (36.5%) were procured from Chengdu Kelong Chemical Co. Hexamethyldisilazane (HMDS, 98%) was acquired from Aladdin Chemistry. Deionized water was employed, and all chemicals were used without additional purification.

Sols synthesis

The colloidal silica suspension was prepared by the Stöber method[30]. In a typical synthesis, 26.6 mL TEOS was added in 263.2 mL ethanol at ambient temperature, followed by mixed with 9.6 mL aqueous ammonia, and the mixture was stirred for 6 h at 40 °C. The resulting sol was aged at ambient temperature for 12 h, which was named Sol A.

For preparation of soluble organic polysiloxane named Sol B, 22.2 mL TEOS was added in 217.8 mL ethanol at ambient temperature, and then simultaneously mixed with 7.2 mL deionized water and 0.034 mL concentrated hydrochloric acid. The mixture underwent stirring for 6 h at 40 °C, followed by aging for 12 h.

After reflux condensation in 5 h with effective removal of ammonia for Sol A, a composite sol named Sol C was prepared by mixing Sol A and Sol B in a volume ratio of 9 to 1.

Furthermore, 19.96 mL TEOS and 1.88 mL HMDS were added in 219.6 mL ethanol at ambient temperature, and then mixed with 1.27 mL aqueous ammonia. The resulting mixture was stirred for 6 h at 40 °C and further aged for 12 h. Afterwards, the solution was then diluted by adding absolute ethanol with the same volume before film deposition, named Sol D.

Films preparation

The SiO_2-based AR film fabrication involved the following steps: initially, K9 glass substrates firstly were cleaned in ethanol for 10 min, followed by cleaned in acetone for 5 min and air blowing. Then, the SiO_2 sol was coated onto the K9 glass substrate at a designed pulling speed. After dipped in the sol, the pre-cleaned substrate was kept for 5 sec. First, for the preparation of the monolayer film, the blank substrate was coated with Sol C at a pulling speed of 80 mm/min. In the process of fabricating the bilayer film, the initial step involved depositing Sol C on the blank substrate at a constant pulling speed to form the bottom layer. Subsequently, the upper layer was coated with Sol D at a similar speed. Finally, both SiO_2-based AR films were then dried at 60 °C.

Characterization

The morphology of SiO_2 sols was examined through transmission electron microscope (TEM) images captured with a Tecnai G2 F20S-TWIN TEM operating at an acceleration voltage of 200 kV. The microstructural analysis of both the film surface and thickness cross-section was conducted by utilizing a field emission scanning electron microscope (FESEM, SUPRA® 55, Germany) Atomic Force Microscopy (AFM) analysis of the films was conducted by using the SPA-300HV scanning probe microscope under ambient conditions, specifically employing noncontact mode. The transmittance spectra of the anti-reflective films were measured by using a UV-Vis-NIR Infrared spectrophotometer (Mapada, UV-3100PC) around a wavelength range from 400 to 1600 nm. The measurement of water contact angles (WCAs) on film surfaces was conducted by employing a JC2000C contact angle/interface system at ambient temperature. The refractive indices of the films deposited on blank substrates were measured by using a spectroscopic ellipsiometer (SENTECH SE850 UV). The Cauchy model ($n(\lambda)=A + B/\lambda^2 + C/\lambda^4$) was applied in the experimental range spanning from 400 to 1600 nm, with an incidence angle of 70°. The Laser-Induced Damage Threshold (LIDT) in the one-on-one scenario was evaluated in accordance with ISO 21254 standards, employing a Gaussian-shaped 1ω Nd: YAG laser (1064 nm, 10 ns pulse duration). Measurements were conducted at ten discrete locations for each film, employing normal incidence and utilizing an effective spot area on the sample surface of approximately 0.081 mm^2. The assessment of damage involved a comparative analysis of areas subjected to laser irradiation before and after the process, according to utilizing an in-situ camera. Damage was deemed to have transpired when the film surface exhibited irreversible alterations subsequent to laser exposure[31].

RESULTS AND DISCUSSION

TEM was first used to reveal the nanostructures of prepared products. In Fig. 1a, the colloidal silica suspension (Sol A) is in the form of uniform nanoparticles of approximately 15 nm. As seen from Fig. 1b, the soluble organic polysiloxane (Sol B) tends to form linear floccules. When Sol A and Sol B were proportionally mixed in a 9:1 volume ratio, Fig. 1c shows the formation of a chemically crosslinked monolayer, which would be beneficial for the deposition of the bottom layer. The upper layer of the bilayer film was deposited from Sol D (Fig. 1d), presenting a nanonetwork structure. It was said that the sols were hydrolysed by TEOS molecules with hydrochloric acid or ammonia as the catalyst. The previous reaction could be demonstrated by the equation (Eq. 1)[32]:

$$nSi(OC_2H_5)_4+2nH_2O\rightarrow nSiO_2+4nC_2H_5OH \quad (1)$$

The first step involves the silicon-ethoxy group hydrolysis, resulting in the formation of silanol. Subsequently, the reaction could follow two pathways, depending on the choice of an acidic or basic catalyst. Under acidic catalysis, an initial soluble intermediate product is generated, in which there are a number of siloxane chains with hydroxyl and alkoxy groups. This ultimately leads to the formation of linear floccules, as illustrated in Fig. 1b and Eq. 2–3.

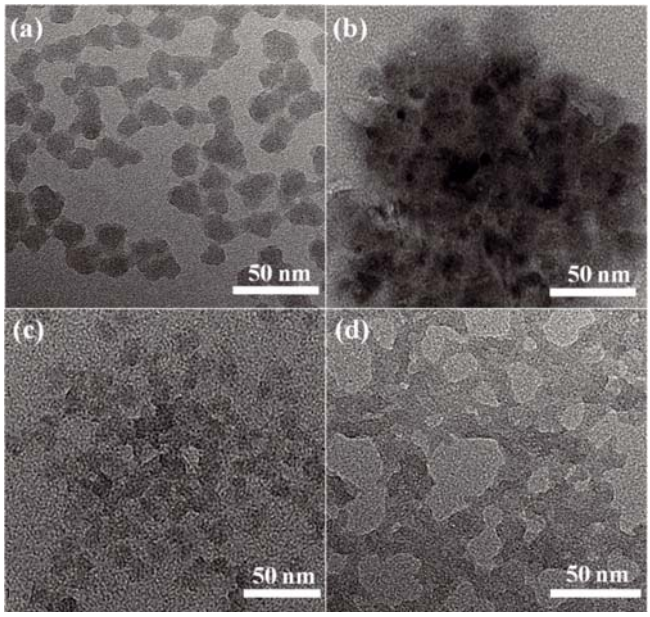

Figure 1. TEM images of (a) the colloidal silica suspension (Sol A), (b) the soluble organic polysiloxane (Sol B), (c) the composite sol (Sol C) and (d) the organic-inorganic hybrid sol (Sol D)

$$2(C_2H_5O)_3SiOH \xrightarrow{acid} (C_2H_5O)_3SiOSi(C_2H_5O)_3 + H_2O \quad (2)$$

$$2(C_2H_5O)_3SiOSi(C_2H_5O)_3 + 2H_2O \rightarrow 4SiO_2 + 6C_2H_5OH \quad (3)$$

Under basic catalysis, the reaction occurs at ambient temperature, resulting in the eventual formation of a colloidal silica suspension. These silica particles exhibit a spherical shape and are nearly uniform in size, as depicted in Fig. 1(a). This observation aligns closely with the findings reported by Thomas[33].

$$(C_2H_5O)_3SiOH + 2NH_3 \cdot H_2O \xrightarrow{base} (C_2H_5O)_2Si(OH)_2 + \quad (4)$$
$$+ 2C_2H_5OH + 2NH_3 \cdot H_2O$$

$$2(C_2H_5O)_2Si(OH)_2 \rightarrow Si(OH)_4 + 4C_2H_5OH \quad (5)$$

$$4Si(OH)_4 \rightarrow 4SiO_2 + 8H_2O \quad (6)$$

Thus, two distinct reaction pathways lead to the ultimate production of silica. The base-catalyzed hydrolysis is used to generate a colloidal silica suspension (Sol A), and the acid-catalyzed hydrolysis is presented to obtain the soluble organic polysiloxane (Sol B).

Therefore, the mixture of Sol A and Sol B could lead to chemical crosslinking structures (Fig. 1c), in which silica spheres were chemically bonded with the soluble organic siloxane. The relative quantities of the two silica types would influence porous structure and optical property. Fig. 1c suggests that the porous structure could be maintained in which the silica spheres were chemically bonded in an open siloxane crosslinking framework. Owing to chemical bonding between silica spheres, the film was anticipated to exhibit the impressive abrasion resistance.

Meanwhile, the surface of silica nanoparticles in Sol A features numerous hydrophilic OH groups (Eq. 4). These groups could readily adsorb organic compounds or water from the atmospheric environment. To address the limitation, the HMDS was added in the synthesis of Sol D. The addition facilitated the reaction of OH groups with HMDS molecules, leading to the conversion of a significant portion of hydrophilic OH groups into hydrophobic CH_3 groups, as illustrated by the following reaction (Eq. 7) [33]:

$$2OH + (CH_3)_3SiNHSi(CH_3)_3 \rightarrow 2\text{-}O\text{-}Si(CH_3)_3 + NH_3 \quad (7)$$

Thus, the above reaction described resulted in the conversion of the hydrophilic SiO_2 nanoparticles to the hydrophobic ones.

Figure 2 shows surface morphology of both monolayer and bilayer SiO_2 films by SEM images. In Fig. 2(a), the monolayer film, the thickness of which is 105 nm (Fig. 2b) exhibits a porous surface, forming the bottom layer. The porous structure is agreed with the crosslinking framework observed in TEM (Fig. 1c) when the alkali-acid sols were mixed in a 9:1ratio. Upon covering the bottom layer with Sol D, the upper layer displayed a coarse surface (Fig. 2c), attributing to the HMDS-modified nanoparticles (Fig. 1d). The upper layer, the thickness of which is 103 nm as shown in Fig. 2d, was deposited onto the bottom layer to create a bilayer film. The bilayer film coated on the K9 glass substrate exhibited differences in visible light reflectance compared to the monolayer one (Fig. 2e and Fig. 2f).

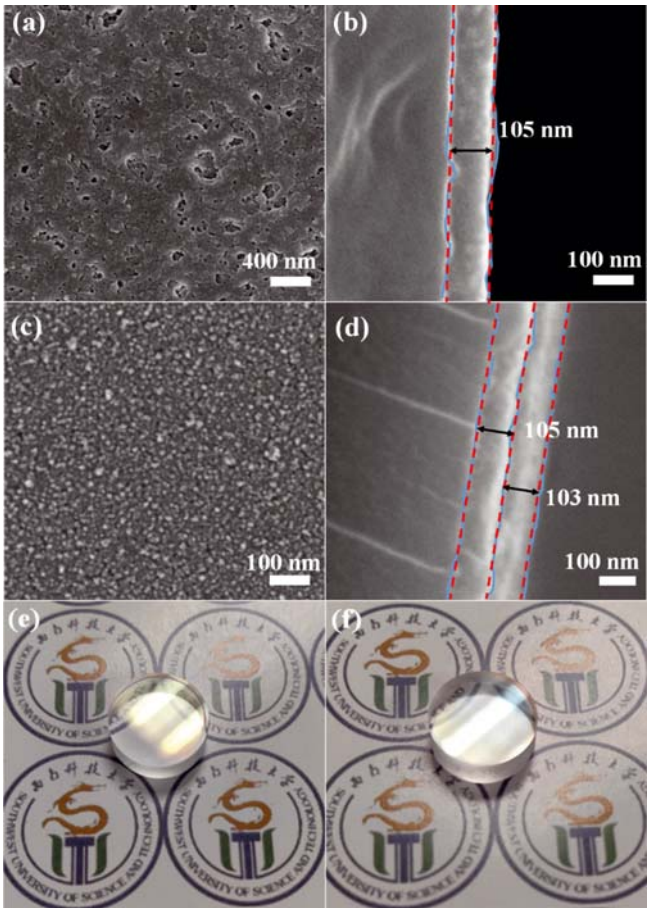

Figure 2. A top-view SEM image (a) and a cross-sectional SEM image (b) of the monolayer film, as well as (c) a top-view SEM image and a cross-sectional SEM image (d) of the bilayer film. Photographs of the monolayer film (e) and the bilayer film (f) coated on K9 glass substrate

Figure 3 presents AFM images depicting the surface characteristics of both the monolayer and bilayer films. The root mean-square (RMS) roughness values for the monolayer and bilayer films were found to be 1.5 nm and 17.7 nm, respectively. Notably, the bilayer film displayed a significantly rougher surface, facilitating the creation of a hydrophobic surface with elevated surface roughness.

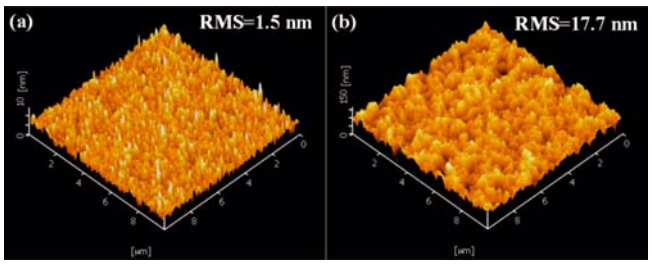

Figure 3. The monolayer surface AFM image (a) and the bilayer surface AFM image (b)

Figure 4 presents refractive indexes of the blank substrate, bottom layer and upper layer, respectively. It could be seen that the refractive index (n) value gradually reduces from the blank substrate to upper layer. Notably, there came a refractive index gradient, offering advantages for anti-reflective objectives[34, 35]. An important achievement was the attainment of a film with a refractive index about 1.25. This film was proved being appropriate as a bottom layer for constructing the multilayer film. Meanwhile, the bottom layer showed the resistance to ethanol scour or dissolution, making sure the efficient deposition of the upper layer.

Due to the evidently lower refractive indexes of the films, they exhibited enhanced AR properties. Thus, as seen from Fig. 5, the transmittance and reflectance

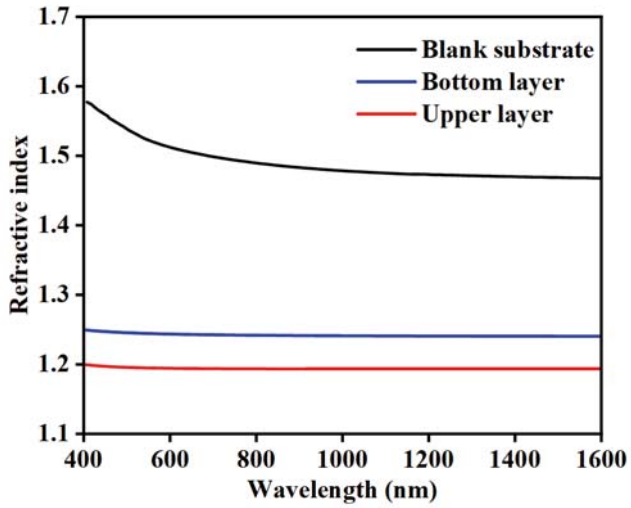

Figure 4. Refractive index of the blank substrate, the bottom layer and the upper layer, respectively

spectra were all measured to demonstrate their AR performance. The transmittance of blank K9 substrate was approximately 92% in the wavelength range of 400 to 1600 nm. The transmittance of the monolayer and bilayer films increased to about 97.3% and 99.5% at 1064 nm, which was consistent with the related reduction in their reflectivity, respectively. This could be attributed to the incorporation of the refractive-index gradient-structure.

According to the above analysis, porous SiO_2 AR films have a tendency to moisture absorption and organic pollution. Because air within the pores is displaced by water and organic compound, the AR film refractive index increases, leading to a reduction in its optical transmittance. To suppressing the moisture adsorption by the film, hydrophilic groups, such as –OH, were replaced by hydrophobic groups, such as $–CH_3$, on the surface of SiO_2 nanoparticles. Thus, the surface of SiO_2

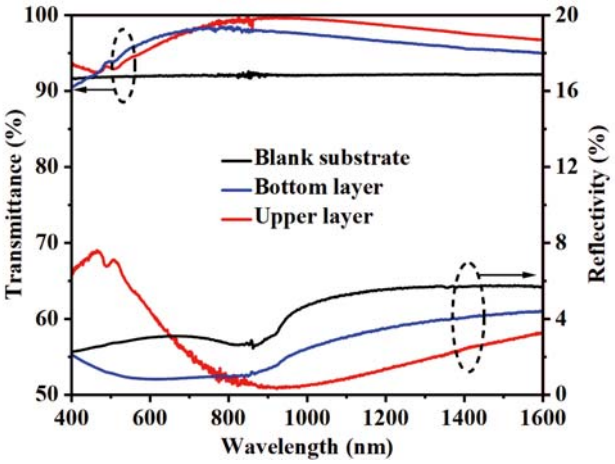

Figure 5. Transmission and reflectance spectra of the blank substrate, the bottom layer and the upper layer, respectively

nanoparticles was modified by the hydrophobic HMDS molecule, serving as the upper layer.

Therefore, the surface wettability of SiO_2 AR films was investigated by testing water contact angles (WCAs), as depicted in Fig. 6. The monolayer film without HMDS modification exhibits high hydrophilicity, the WCA of which is about 36.5° (Fig. 6a). Due to the HMDS modification, the bilayer film displays hydrophobic characteristic, and the WCA is 125.5° (Fig. 6b). The hydrophobicity of the bilayer film is attributed to the introduction of hydrophobic alkyl groups, which enables the bilayer film moisture-resistant property.

Furthermore, As seen from Fig. 7, the LIDT of the monolayer and bilayer films were 19.0 J/cm^2 and 24.7 J/cm^2, respectively. Remarkably, the bilayer film exhib-

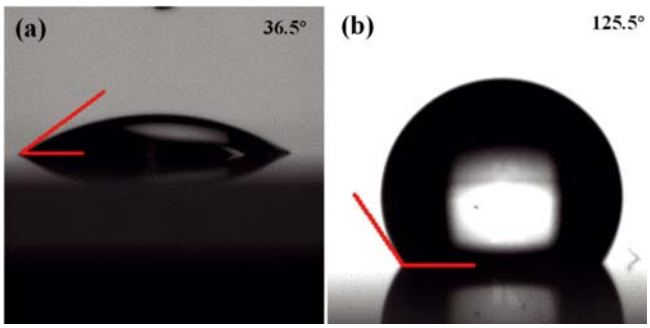

Figure 6. WCAs on the monolayer film surface (a) and the bilayer film surface (b)

ited superior laser damage resistance, highlighting their potential application in laser systems.

The morphological alterations induced by varying laser fluences on SiO_2 AR films are illustrated in Fig. 8. It was seen that the surface of the monolayer film showed deformation by irradiated with a 15.0 J/cm^2 laser fluence (Fig. 8a). When the laser fluence surpassed the LIDT (e.g., 25.0 J/cm^2), it was observed that the phenomenon of peeling off in the damaged area center of the bilayer film (Fig. 8b). Moreover, the peeling-off area was increased in size with a higher laser fluence. As the laser fluence continued to rise, the laser damage penetrated into K9 glass substrate, resulting in shell-like holes. For the bilayer film, surface partial melting was only induced under the low laser fluence (Fig. 8c), while the fusion zone connection to form a foveolate damage area was caused by a high laser fluence

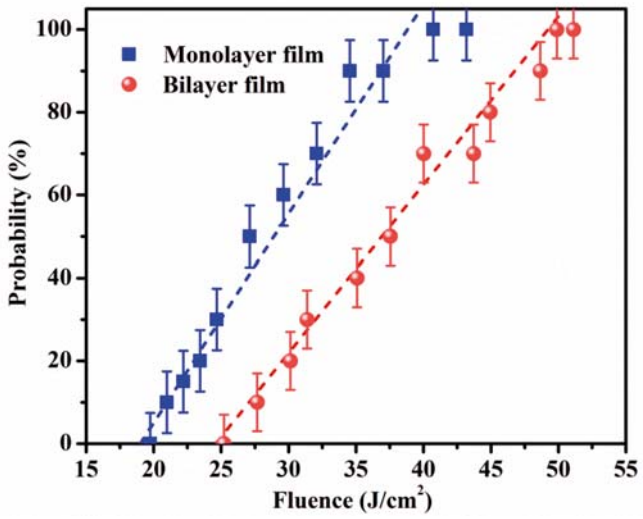

Figure 7. Laser-induced damage probability of the monolayer film (square) and the bilayer film (sphere)

(25.0 J/cm^2) (Fig. 8d). Thus, it could be demonstrated that the laser damage extent of the bilayer film was significantly reduced compared with the monolayer film.

It had been reported that the laser damage was caused by the defect on surface or trapped in the film[36].Thus, the high temperature, which was caused by initiator adsorption under intense laser fluence irradiation, resulted in phase transformation and produced a substantial local pressure. This pressure could deform the SiO_2 film and eventually peel it from the substrate. It was seen that the surface of the bilayer film effectually repulsed moisture (Fig. 6), which was helpful to improve its laser damage resistance. Thus, on one hand, the bilayer film showed well anti-reflective performance, on the other hand, it exhibited high laser damage resistance, which would endow SiO_2 AR films for high-power laser system application.

Previous investigations aiming for high transmittance, often exceeding 98%, have encountered great challenges,

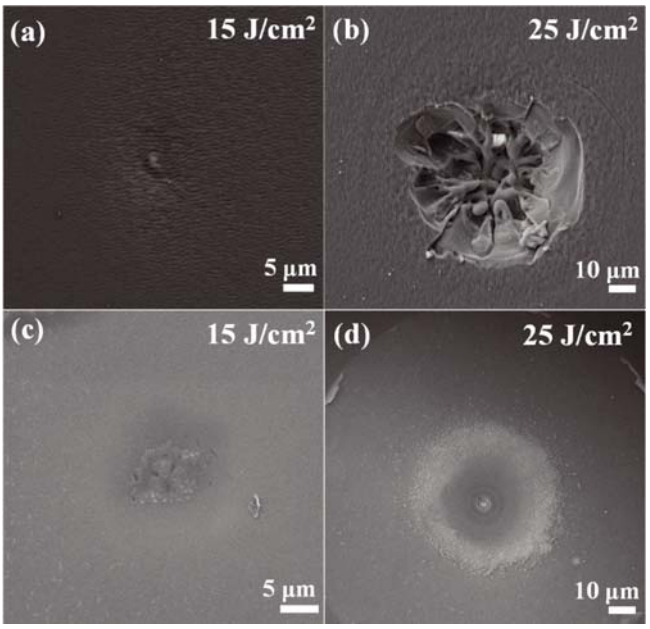

Figure 8. Damage morphology SEM images of the monolayer film under different laser fluence of (a) 15.0 J/cm^2 and (b) 25.0 J/cm^2, respectively. Damage morphology SEM images of the bilayer film under different laser fluence of (c) 15.0 J/cm^2 and (d) 25.0 J/cm^2, respectively

such as the complex preparation methods and relatively low transmittance at 1064 nm[24, 25]. In this study, the refractive-index gradient SiO_2 film achieved 99.5% transmittance at 1064 nm by a sol-gel procedure with the low cost and simple processes. Furthermore, its laser damage resistance (24.7 J/cm^2) irradiated by a 1064 nm laser exceeded those reported in other studies (below 20 J/cm^2)[37–39]. The notable enhancement of laser damage resistance was due to the hydrophobic upper layer surface.

CONCLUSIONS

In summary, the refractive-index gradient SiO_2 antireflective films were prepared through a straightforward sol-gel procedure. For the crucial bottom layer design, the porous structure with chemical bonding between nanoparticles was formed, which made sure the film resistance to ethanol dissolution. Due to HMDS modification, the upper layer was hydrophobic. It was demonstrated that the bilayer film exhibited superior antireflective property (99.5% @ 1064 nm) and a laser damage resistance (24.7 J/cm^2). In a word, the present refractive-index gradient SiO_2 films, featuring superior antireflective property and enhanced laser-induced damage threshold, were easily fabricated through a sol-gel procedure, showcasing great potential in high-power laser systems.

ACKNOWLEDGEMENTS

This work was supported by National Natural Science Foundation of China (Grant No. U2230119), Scientific Research Fund of Sichuan Provincial Science and Technology Department (2022NSFSC0333), 2022 Central Guidance on Local Science and Technology Development Projects (2022ZYDF073), Outstanding Youth Fund of Sichuan Province (22JCQN0005) and Key Laboratory of Icing and Anti/De-icing of CARDC (Grant No. IADL 20220409).

LITERATURE CITED

1. Hurricane, O.A., Patel, P.K., Betti, R., Froula, D.H., Regan, S.P., Slutz, S.A., Gomez, M.R. & Sweeney, M.A. (2023). Physics principles of inertial confinement fusion and US program overview. *Rev. Mod. Phys.* 95(2), 025005. DOI: 10.1103/RevModPhys.95.025005.

2. Kraus, M., Diao, Z., Weishaupt, K., Spatz, J.P., Täschner, K., Bartzsch, H., Schmittgens, R. & Brunner, R. (2019). Combined 'moth-eye'structured and graded index-layer antireflecting coating for high index glasses. *Opt. Express* 27(24), 34655–34664. DOI: 10.1364/OE.27.034655.

3. Choi, K., Yoon, Y., Jung, J., Ahn, C.W., Lee, G.J., Song, Y.M., Ko, M.J., Lee, H.S., Kim, B. & Kang, I.S. (2017). Super-Antireflective Structure Films with Precisely Controlled Refractive Index Profile. *Adv. Opt. Mater.* 5(3), 1600616. DOI: 10.1002/adom.201600616.

4. Rostami, M., Pirvaram, A., Talebzadeh, N. & O'Brien, P.G. (2021). Numerical evaluation of one-dimensional transparent photonic crystal heat mirror coatings for parabolic dish concentrator receivers. *Renew. Energ*. 171, 1202–1212. DOI: 10.1016/j.renene.2021.03.007.

5. Shanmugam, N., Pugazhendhi, R., Madurai Elavarasan, R., Kasiviswanathan, P. & Das, N. (2020). Anti-reflective coating materials: A holistic review from PV perspective. *Energy* 13(10), 2631. DOI: 10.3390/en13102631.

6. Zhang, X., Lu, Q., Cheng, Y., Liu, L., Shan, Y., Zhang, G. & Li, D. (2019). Moth-eye-like antireflection coatings based

on close-packed solid/hollow silica nanospheres. *J. Sol-Gel Sci. Technol*. 90, 330–338. DOI: 10.1007/s10971-018-04912-1.

7. Kim, M.S., Yeo, J.E., Choi, H., Chang, S., Kim, D.H. & Song, Y.M. (2023). Evolution of natural eyes and biomimetic imaging devices for effective image acquisition. *J. Mater. Chem. C* 11(36), 12083–12104. DOI: 10.1039/D3TC01883K.

8. Stanciu, S.G., König, K., Song, Y.M., Wolf, L., Charitidis, C.A., Bianchini, P. & Goetz, M. (2023). Toward next-generation endoscopes integrating biomimetic video systems, nonlinear optical microscopy, and deep learning. *Biophys. Rev.* 4(2), 021307. DOI: 10.1063/5.0133027.

9. Liu, Z., Lian, Z., Ren, W., Xu, J., & Yu, H. (2023). Hierarchically structured stainless-steel surfaces with superior superhydrophobicity and anti-reflection. *Materials Letters* 350, 134917. DOI: 10.1016/j.matlet.2023.134917.

10. Wu, P., Xue, Z., Yu, T. & Penkov, O. V. (2023). Transparent Self-cleaning Coatings: A Review. *Coatings* 13, 1270. DOI: 10.20944/preprints202306.0563.v1

11. Jiao, Z., Wang, Z., Wang, Z. & Han, Z. (2023). Multifunctional Biomimetic Composite Coating with Antireflection, Self-Cleaning and Mechanical Stability. *Nanomaterials* 13(12), 1855. DOI: 10.3390/nano13121855.

12. Wang, D., Li, Y., Wen, Y., Li, X. & Du, X. (2021). Simple and low cost fabrication of large area nanocoatings with mechanical robustness, enhanced broadband transmittance and antifogging. *Colloids Surf. A Physicochem. Eng. Asp.* 629, 127522. DOI: 10.1016/j.colsurfa.2021.127522.

13. Xi, R., Wang, Y., Li, X., Zhang, X. & Du, X. (2020). A facile strategy to form three-dimensional network structure for mechanically robust superhydrophobic nanocoatings with enhanced transmittance. *J. Colloid Interf. Sci.* 563, 42–53. DOI: 10.1016/j.jcis.2019.12.049.

14. Dobrowolski, J.A., Poitras, D., Ma, P., Vakil, H. & Acree, M. (2002). Toward perfect antireflection coatings: numerical investigation. *Appl. Optics* 41(16), 3075–3083. DOI: 10.1364/AO.41.003075.

15. Tajima, N., Murotani, H. & Matsudaira, T. (2023). Optical multicoating using low-refractive-index SiO_2 optical thin films deposited by sputtering and electron beam evaporation. *Thin Solid Films* 776, 139824. DOI: 10.1016/j.tsf.2023.139824.

16. Feng, C., Zhang, P., Zhang, W., Sun, J., Wang, J., Zhao, Y. & Shao, J. (2023). "Interface-free" ultrabroadband antireflection film based on nanorod structure with continuous change in refractive index. *Opt. Mater.* 141, 113965. DOI: 10.1016/j.optmat.2023.113965.

17. Pfeiffer, K., Ghazaryan, L., Schulz, U. & Szeghalmi, A. (2019). Wide-angle broadband antireflection coatings prepared by atomic layer deposition. *ACS Appl. Mater. Interf.* 11(24), 21887–21894. DOI: 10.1021/acsami.9b03125.

18. He, M., Wang, P., Xiao, P., Jia, X., Luo, J. & Jiang, B. (2023). Hollow silica nanospheres synthesized by one-step etching method to construct optical coatings with controllable ultra-low refractive index. *Colloid Surf. A* 670, 131433. DOI: 10.1016/j.colsurfa.2023.131433.

19. Wu, H., Liu, C., Zhu, Z., Shao, Y., Lin, J., Wen, J., Wang, H., Zhang, Y., Liang, T., Shao, Y. & Shen, W. (2023). Nanoporous Silicon Dioxide Films for Large Area and Low-Cost Fabrication of Ultra-Low Refractive Index Coatings. *ACS Appl. Nano Mater.* 6(17), 15437–15444. DOI: 10.1021/acsanm.3c01963.

20. Ye, L., Zhang, X., Zhang, Y., Li, Y., Zheng, W. & Jiang, B. (2016). Three-layer tri-wavelength broadband antireflective coatings built from refractive indices controlled silica thin films. *J. Sol-Gel Sci. Technol.* 80, 1–9. DOI: 10.1007/s10971-016-4051-y.

21. Ziming, C., Fuqiang, W., Dayang, G., Huaxu, L. & Yong, S. (2020). Low-cost radiative cooling blade coating with ultrahigh visible light transmittance and emission within an "atmospheric window". *Sol. Energ. Mater. Sol. C.* 213, 110563. DOI: 10.1016/j.solmat.2020.110563.

22. Joshi, D.N., Atchuta, S.R., Reddy, Y.L., Kumar, A.N. & Sakthivel, S. (2019). Super-hydrophilic broadband anti-reflective coating with high weather stability for solar and optical applications. *Sol. Energ. Mater. Sol. C.* 200, 110023. DOI: 10.1016/j.solmat.2019.110023.

23. Lu, M., Liu, Q., Wang, Z., Zhang, X., Luo, G., Lu, J., Zeng, D., Zhao, X. & Tian, S. (2023). Facile preparation of porous SiO_2 antireflection film with high transmittance and hardness via self-templating method for perovskite solar cells. *Mater. Today Chem.* 29, 101473. DOI: 10.1016/j.mtchem.2023.101473.

24. Yoldas, B.E. & Partlow, D.P. (1985). Formation of broad band antireflective coatings on fused silica for high power laser applications. *Thin Solid Films* 129(1-2), 1–14. DOI: 10.1016/0040-6090(85)90089-6.

25. Ding, R., Cui, X., Zhang, C., Zhang, C. & Xu, Y. (2015). Tri-wavelength broadband antireflective coating built from refractive index controlled MgF_2 films. *J. Mater. Chem. C* 3(13), 3219–3224. DOI: 10.1039/C4TC02542C.

26. Li, X., Zou, L., Wu, G. & Shen, J. (2014). Laser-induced damage on ordered and amorphous sol-gel silica coatings. *Opt. Mater. Express* 4(12), 2478–2483. DOI: 10.1364/OME.4.002478.

27. Lin, P., Mah, M., Randi, J., DeFrances, S., Bernot, D. & Talghader, J.J. (2023). High average power optical properties of silica aerogel thin film. *Thin Solid Films*, 768, 139722. DOI: 10.1016/j.tsf.2023.139722.

28. Fan, Q., Liu, H., Jia, X., Yan, L. & Jiang, B. (2022). Study on the Hydrophobic Modification of MTES/NH_3 Vapor Surface Treatment for SiO_2 Broadband Anti-Reflection Coating. *Mater.* 15(3), 912. DOI: 10.3390/ma15030912.

29. Wang, X. & Shen, J. (2012). A review of contamination-resistant antireflective sol–gel coatings. *J. Sol-Gel Sci. Technol.* 61, 206–212. DOI: 10.1007/s10971-011-2615-4.

30. Jiang, X., Tang, X., Tang, L., Zhang, B. & Mao, H. (2019). Synthesis and formation mechanism of amorphous silica particles via sol–gel process with tetraethylorthosilicate. *Ceram. Inter.* 45(6), 7673–7680. DOI: 10.1016/j.ceramint.2019.01.067.

31. Dong, S.Y., Jiao, H.F., Wang, Z.S., Zhang, J.L. & Cheng, X.B. (2022). Interface and defects engineering for multilayer laser coatings. *Prog. Surf. Sci.* 97(3), 100663. DOI: 10.1016/j.progsurf.2022.100663.

32. Rao, A.V., Latthe, S.S., Nadargi, D.Y., Hirashima, H. & Ganesan, V. (2009). Preparation of MTMS based transparent superhydrophobic silica films by sol–gel method. *J. Colloid Interf. Sci.* 332(2), 484–490. DOI: 10.1016/j.jcis.2009.01.012.

33. Thomas, I.M. (1992). Method for the preparation of porous silica antireflection coatings varying in refractive index from 1.22 to 1.44. *Appl. Optics* 31(28), 6145–6149. DOI: 10.1364/AO.31.006145.

34. Wang, J., Wang, T., Wang, X., Yang, W., Wang, Z., Li, M. & Shi, L. (2023). Effect of applied voltage on localized deposition of silicon dioxide-like films on stainless steel using atmospheric pressure microplasma jet. *Plasma Chem. Plasma P.* 43(4), 879–899. DOI: 10.1007/s11090-023-10332-z.

35. Zhang, J., Yuan, J., Tian, P., Mao, J. & Zhang, Q. (2023). Preparation of gradient refractive index films on glass surface and its anti-reflection properties. *J. Alloy. Compd.* 972, 172831. DOI: 10.1016/j.jallcom.2023.172831.

36. Zhao, Y., Gao, W., Shao, J. & Fan, Z. (2004). Roles of absorbing defects and structural defects in multilayer under single-shot and multi-shot laser radiation. *Appl. Surf. Sci.* 227(1–4), 275–281. DOI: 10.1016/j.apsusc.2003.12.006.

37. Song, Z., Cheng, X., Ma, H., Zhang, J., Ma, B., Jiao, H. & Wang, Z. (2017). Influence of coating thickness on laser-induced damage characteristics of anti-reflection coatings irradiated by 1064 nm nanosecond laser pulses. *Appl. Optics* 56(4), C188-C192. DOI: 10.1364/AO.56.00C188.

38. Chen, X.Q., Zu, X.T., Zheng, W.G., Jiang, X.D., Lü, H.B., Ren, H., Zhang, Y.Z. & Liu, C.M. (2006). Experimental research of laser-induced damage mechanism of the sol-gel SiO_2 and IBSD SiO_2 thin films. *Acta Phys. Sin-Chin. Ed.* 55(3), 1201–1206. DOI: http://wulixb.iphy.ac.cn/CN/Y2006/V55/I3/1201.

39. Zhang, L., Xu, Y., Huang, Z.X., Yang, D.J., Jiang, X.D., Wu, D., Sun, Y. H. &Wei, X.F. (2005). Effect of PEG on laser damage of sol-gel SiO_2 anti-reflective coating. *High Power Laser Part. Beams* 17(05), 669–672. DOI: CNKI:SUN:QJGY.0.2005-05-008.